




 Cite this: *RSC Adv.*, 2020, 10, 23331

# *Ex situ* catalytic fast pyrolysis of soy sauce residue with HZSM-5 for co-production of aromatic hydrocarbons and supercapacitor materials†

 Kai Li,  Dana Bolatibieke, Shi-guan Yang, Bo Wang, Dong-hong Nan and Qiang Lu \*

A promising approach is proposed for the efficient conversion of soy sauce residue (SSR) into aromatic hydrocarbons and a supercapacitor electrode material by *ex situ* catalytic fast pyrolysis (CFP) technology with HZSM-5. The thermal decomposition behaviors of SSR were first investigated *via* thermogravimetry (TG) and pyrolysis-gas chromatography/mass spectrometry (Py-GC/MS) analyses. The *ex situ* CFP of SSR was conducted to elucidate the aromatic hydrocarbons production under different pyrolysis temperatures and HZSM-5-to-SSR (HZ-to-SSR) ratios using both Py-GC/MS and lab-scale instruments. The results indicated that the aromatic hydrocarbons reached the maximal yields of 22.20 wt% from Py-GC/MS with an HZ-to-SSR ratio of 11 at 650 °C, and 17.61 wt% from the lab-scale device with an HZ-to-SSR ratio of 2, respectively. The as-obtained yield of aromatic hydrocarbons was far higher than those obtained from typical lignocellulosic biomass materials, confirming that SSR is a promising material for aromatics production. The pyrolytic solid product collected with this method was further activated by KOH to synthesize N-doped activated carbon (NAC) for supercapacitors. The physicochemical analysis showed that NAC possessed N-incorporated hierarchical pores, and exhibited a promising capacitance of 274.5 F g<sup>-1</sup> at 1 A g<sup>-1</sup>.

 Received 3rd May 2020  
 Accepted 3rd June 2020

DOI: 10.1039/d0ra03993d

[rsc.li/rsc-advances](http://rsc.li/rsc-advances)

## 1. Introduction

Soy sauce is a popular seasoning worldwide and is mainly made from soybeans, grains, water and salt. Soy sauce residue (SSR) is an important byproduct of soy sauce fermentation, which has a dark brown color, unpleasant awful smell and complicated constituents, including proteins, lipids, crude fiber, salt, and so on.<sup>1</sup> SSR is chiefly employed as livestock feed, especially for pigs. Nevertheless, this application is currently becoming less ideal because of the abundant salts (14–18%) and terrible palatability of SSR, which is not conducive to the growth of pigs, and even leads to the death of pigs.<sup>2</sup> Recently, some new utilization methods of SSR were proposed, such as the separation of proteins,<sup>3</sup> isoflavone,<sup>4</sup> and so on. However, none of these methods have been commercially utilized so far, primarily because of the complicated process, high cost and low yield of targeted products. Therefore, it is imperative to develop new efficient methods to achieve the clean and high-valued utilization of SSR.

Fast pyrolysis technology provides an efficient and economical way to achieve the quick conversion of organic solid materials into various pyrolytic products.<sup>5,6</sup> The pyrolytic liquid product can be used as liquid fuels or raw chemical materials.<sup>7</sup> The solid product can be upgraded into soil amendments,<sup>8</sup> activated carbon,<sup>9</sup> and supercapacitor electrode materials.<sup>10,11</sup> To further ameliorate the quality of pyrolytic products, catalytic fast pyrolysis (CFP) enables the selective production of targeted compounds,<sup>11–13</sup> which might be a promising way for the utilization of SSR. However, few relevant studies have been performed for the CFP of SSR at present.

In light of the complicated constituents of SSR, catalyst selection is vital for its CFP conversion.<sup>14</sup> HZSM-5 is usually regarded as an ideal option for the CFP of biomass,<sup>15</sup> due to its thermal stability, high shape selectivity and excellent selectivity for aromatic hydrocarbons, as well as the strong adaptability of feedstock. Mihalcik *et al.*<sup>16</sup> confirmed the effective capability of HZSM-5 on the aromatic production using the CFP of different lignocellulosic biomass, including switchgrass, corn cobs, oak and their primary components. Thangalazhy-Gopakumar *et al.*<sup>17</sup> investigated the CFP of algae (*C. vulgaris*) with HZSM-5 and obtained aromatic hydrocarbons with the highest carbon yield of 25.8 wt%. Li *et al.*<sup>18</sup> adopted HZSM-5 to the CFP of pine with calcium formate and the yield of monocyclic aromatic hydrocarbons (MAHs) reached 10.65 wt%. Therefore, based on the previous studies, it is reasonable to infer that HZSM-5 might

National Engineering Laboratory for Biomass Power Generation Equipment, North China Electric Power University, Beijing 102206, China. E-mail: [qianglu@mail.usc.edu.cn](mailto:qianglu@mail.usc.edu.cn); [qlu@ncepu.edu.cn](mailto:qlu@ncepu.edu.cn); Tel: +86-10-61772030

† Electronic supplementary information (ESI) available. See DOI: 10.1039/d0ra03993d



also be effective for the CFP of SSR to obtain aromatic hydrocarbons as the major liquid product.

In addition to the liquid product, the utilization of the pyrolytic solid product is also important to the economy of the CFP technology. Recently, the preparation of supercapacitor materials from biomass has garnered increasing attention.<sup>19</sup> However, the supercapacitors prepared from conventional lignocellulosic biomass only exhibited moderate capacitive performance because of the limited active sites.<sup>20</sup> The incorporation of heteroatoms, especially N, into carbon material is an effective way to improve the capacitive performance.<sup>21</sup> Generally, N incorporation could be achieved by additional ammonization or co-pyrolysis with N-abundant substances. Xu *et al.*<sup>22</sup> employed bean dregs as N dopants for co-pyrolysis with rice husk to prepare N-doped activated carbons (NAC) for supercapacitors, the corresponding capacitance ( $C_g$ ) was 319 F g<sup>-1</sup> at 0.2 A g<sup>-1</sup>. However, the NAC obtained in this way is usually heterogeneous. To overcome this deficiency, many researchers have pursued the preparation of NAC directly from N-rich materials, such as egg shells,<sup>18</sup> squid gladius chitin,<sup>23</sup> camellia oleifera shells,<sup>24</sup> *etc.* The NAC prepared from squid gladius chitin possessed an excellent  $C_g$  of 204 F g<sup>-1</sup>, while the  $C_g$ s of NACs obtained from egg shells and camellia oleifera shells were 191 F g<sup>-1</sup> and 205 F g<sup>-1</sup>, respectively. Since SSR is abundant in nitrogen due to its high protein content,<sup>1</sup> it might have the unique advantage to produce NAC for supercapacitors.

Therefore, in this study, the *ex situ* CFP of SSR over HZSM-5 was developed to concurrently produce aromatic hydrocarbons and a supercapacitor electrode material. Considering that the thermal decomposition behaviors of SSR are not well known at present, thermogravimetric (TG) and pyrolysis-gas chromatography/mass spectrometry (Py-GC/MS) analyses were first executed to investigate the thermal degradation of SSR and reveal the pyrolysis kinetics and product distribution.<sup>25</sup> Afterwards, *ex situ* CFP tests of SSR with HZSM-5 were executed *via* both Py-GC/MS and a scale-up device. The effects of the pyrolytic reaction temperature as well as the HZSM-5-to-SSR (HZ-to-SSR) ratio on the product formation were studied comprehensively to maximize the yield of aromatic hydrocarbons. Moreover, the pyrolytic solid product was directly activated by KOH to synthesize NAC for supercapacitor materials.

## 2. Experimental

### 2.1 Materials

SSR was provided by a soy sauce factory in Sichuan Province, China. The received SSR was oven-dried, ground and sieved to obtain dry particles (<0.1 mm) as the feedstock. The ultimate analysis was executed using an elemental analyzer. The proximate analysis was executed based on the national standard, *i.e.*, GB/T 28731-2012. The Van Soest method was adopted to determine the cellulose, hemicellulose and lignin contents. The protein, salt (NaCl), and fat contents were measured according to the relevant national standards in food fields, *viz.* GB/T 5009.5-2016, GB/T 12457-2008 and GB/T 5009.6-2016, respectively. All the above analyses were conducted on the dry basis. All results met the standard deviations specified in the corresponding standards.

HZSM-5 (Si/Al = 27) was provided by Nankai University and calcined at 500 °C before use.

### 2.2 Thermogravimetric experiments and kinetics analysis

The thermal decomposition behaviors of SSR were determined *via* a thermogravimetric analyzer (STA6000). In each run, about 10 mg SSR was used. Measurements were executed under N<sub>2</sub> flow from 50 °C to 700 °C at 5, 10, 20 and 40 °C min<sup>-1</sup>.

The pyrolysis reaction kinetics of SSR can be expressed as follows:<sup>26</sup>

$$\frac{d\alpha}{dt} = A e^{-\frac{E}{RT}} f(\alpha) \quad (1)$$

wherein,  $\alpha$ ,  $A$ ,  $R$ ,  $T$ , and  $E$  stand for the conversion degree of the sample, pre-exponential factor, gas constant, absolute temperature, and activation energy, respectively.

$$\alpha = \frac{m_0 - m_t}{m_0 - m_\infty} \quad (2)$$

where  $m_0$ ,  $m_\infty$ , and  $m_t$  refer to the weight of SSR at the beginning, final and time  $t$ , respectively.

Considering the constant heating rate,  $\beta = dT/dt$ , eqn (1) can be written as follows:

$$f(\alpha) = \int_0^\alpha \frac{d\alpha}{1-\alpha} = \int_0^T \frac{A}{\beta} \exp\left(-\frac{E}{RT}\right) dT \quad (3)$$

The Flynn-Wall-Ozawa (FWO) and Kissinger-Akahira-Sunose (KAS) methods were employed to calculate the kinetics. For the FWO method, under the same condition of  $\alpha$ , the value of  $f(\alpha)$  does not change with the different heating procedures, thus a more reliable  $E$  can be obtained without introducing the dynamic model function. The general expression of FWO is as follows:

$$\ln \beta = \ln\left(\frac{k_0 E}{R f(\alpha)}\right) - 5.331 - 1.052 \frac{E}{RT} \quad (4)$$

The same conversion value  $\alpha$  is selected at different heating rates, and  $T^{-1}$  is linearly regressed by  $\ln \beta$ . The corresponding  $E$  can be obtained directly according to the slope of the fitting line.

The KAS method is a typical integral method, expressed by step-by-step integration with the general expression as follows:

$$\ln\left(\frac{\beta}{T^2}\right) = \ln\left(\frac{k_0 R}{E f(\alpha)}\right) - \frac{E}{RT} \quad (5)$$

Under different heating rates, for a given conversion  $\alpha$ , according to formula (5),  $\ln(\beta/T^2)$  and  $T^{-1}$  can be used in linear regression, and the corresponding  $E$  can be attained according to the slope.

### 2.3 Py-GC/MS tests

A micropyrolyzer (CDS 5200HP) was adopted to execute the *ex situ* CFP of SSR with HZSM-5 and the obtained organic volatiles were immediately delivered to GC/MS (Clarus 560) for on-line

analysis. In each run, the usage of SSR was 0.20 mg, while the HZSM-5 amount was determined by the HZ-to-SSR ratios (mass ratios) of 5, 7, 9, 11 and 13, respectively. The SSR was loaded into the quartz tube with HZSM-5 on both sides. The as-prepared tubes were pyrolyzed for 20 s at designated temperatures (500–700 °C). All the important parameters in the tests were determined by exploratory experiments. The yields of aromatic hydrocarbons were quantified by the external standard calibration method. The details of the Py-GC/MS tests were demonstrated in our previous study.<sup>27</sup>

#### 2.4 Lab-scale CFP experiments

A lab-scale device was adopted to execute the *ex situ* CFP experiments of SSR with HZSM-5, as illustrated in the ESI (Fig. S1†).<sup>7</sup> The device was chiefly made up with a vertical heating furnace, a quartz tube reactor, a nitrogen gas cylinder, and a condenser cooled with liquid nitrogen. For the *ex situ* CFP tests, the reactor preplaced with HZSM-5 was heated to 650 °C first, then the SSR was fed in uniformly to be pyrolyzed. For each run, the usage of SSR was 1 g and the amount of HZSM-5 was varied with the HZ-to-SSR ratios of 0.5, 1, 1.5, 2, and 2.5, respectively. The pyrolysis conditions were also determined through exploratory experiments.

The pyrolytic solid and liquid yields could be determined by weighing, while the gas yield was attained by the difference. The solid product could be collected from the reactor and stored for further usage. The water content of the liquid product was measured using a Karl-Fisher moisture analyzer, while the organic compounds were analyzed and quantified using a gas chromatograph.

#### 2.5 Preparation and characterization of NAC

The solid product obtained from the lab-scale CFP test of SSR with an HZ-to-SSR ratio of 2 at 650 °C was collected and subjected to activation with KOH to prepare NAC. Wherein, the pyrolytic solid product was first impregnated with KOH and subsequently activated at 800 °C for 90 min. Afterwards, HCl solution and hot distilled water at about 80 °C were successively used to wash the cooled mixture. Finally, the NAC was attained after drying at 110 °C.

The physicochemical properties of NAC were measured using an X-ray diffractometer (XRD, D8 advance), nitrogen physisorption (ASAP2460) and X-ray photoelectron spectrometer (XPS, Thermo Escalab 250Xi) to characterize the crystallographic structures, porous characteristics, and chemical states of the main elements in NAC.

The electrochemical tests of NAC were executed using a three-electrode system (CHI660E) with 6 M KOH solution as an electrolyte. Wherein, NAC was used to fabricate the working electrode by homogeneously mixing with polytetrafluoroethylene and acetylene black at a mass ratio of 8 : 1 : 1 and pressed on a nickel foam (1 cm × 1 cm). The platinum and saturated calomel were adopted as the counter and reference electrodes, respectively.

The cyclic voltammetry (CV) tests of NAC were measured at 5–100 mV s<sup>-1</sup>. The galvanostatic charge/discharge (GCD) tests

**Table 1** Proximate, ultimate and component analyses of SSR (wt%, in dry basis)

Proximate analysis		Ultimate analysis		Component analysis	
Volatile	76.46	C	47.13	Protein	24.42
Ash	16.39	H	6.29	Fat	10.30
Fixed carbon	7.15	O	25.46	Cellulose	15.98
		N	4.22	Hemicellulose	9.13
		S	0.51	Lignin	5.54
				Salt	10.19

were executed between 1 and 20 A g<sup>-1</sup>. The electrochemical impedance spectroscopy (EIS) was executed at frequencies varied from 0.01 Hz to 100 kHz in 5 mV.

### 3. Results and discussion

#### 3.1 Physicochemical characteristics of SSR

Table 1 illustrates the proximate, ultimate and component analyses of SSR. The contents of the volatile and fixed carbon of SSR were 76.46 wt% and 7.15 wt%, accompanied with a high ash content of 16.39 wt%. The high ash content was also consistent with the high salt content of 10.19 wt%, which could function as a template to control the pore structure of NAC during the activation process.<sup>28</sup> The contents of C (47.13 wt%), H (6.29 wt%), O (25.46 wt%), N (4.22 wt%), and S (0.51 wt%) were identified, showing a lower O content and higher N content

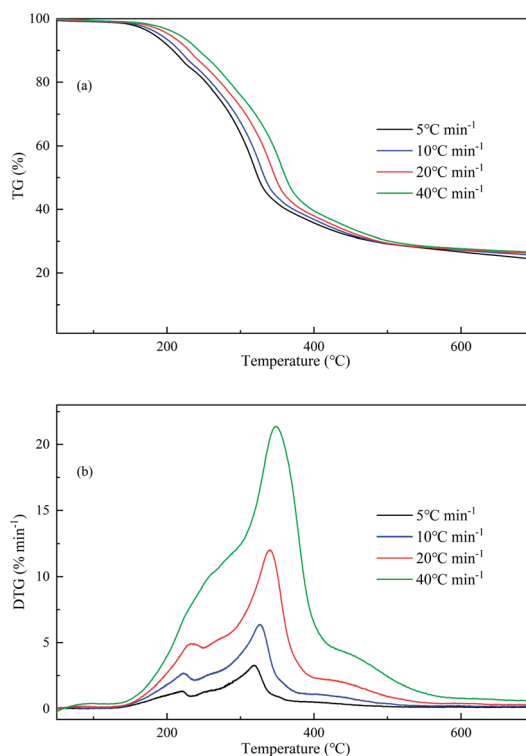


**Fig. 1** TG and DTG curves of SSR.

Table 2 TG and DTG parameters of the stage II in SSR decomposition

$\beta$ ( $^{\circ}\text{C min}^{-1}$ )	$T_i^a$ ( $^{\circ}\text{C}$ )	$T_f^a$ ( $^{\circ}\text{C}$ )	$T_m^b$ ( $^{\circ}\text{C}$ )	$\text{DTG}_{\text{max}}$ ( $\% \text{ min}^{-1}$ )
5	150.0	426.0	318.8	3.27
10	150.4	504.9	326.0	6.35
20	152.2	549.2	339.9	12.01
40	161.6	599.8	348.5	21.37

<sup>a</sup> The initial and final temperatures of the stage II. <sup>b</sup> The corresponding temperature of  $\text{DTG}_{\text{max}}$ .

than typical lignocellulosic biomass, such as rice husk, wheat straw and pine.<sup>29,30</sup> The main contributor to the high N content was the protein component, due to the high average N content in protein of approximately 17 wt%. Compared with conventional lignocellulosic biomass, the proportions of protein (24.42 wt%) and fat (10.30 wt%) in SSR were very high, but those of cellulose (15.98 wt%) and hemicellulose (9.13 wt%) were very low. The low O contents of the former two components were responsible for the low O content in SSR.

### 3.2 Thermogravimetric analysis

Fig. 1 gives the TG and differential thermogravimetric (DTG) curves of SSR. As the heating rates increase, the TG curves shifted toward the high temperature zone because of the increased thermal lag. According to the curves, the thermal decomposition of SSR took place over three stages. Stage I (50–150  $^{\circ}\text{C}$ ) mainly involved the evaporation of water, which was not obvious because dry SSR was employed for analysis. It is notable that the complete drying of biomass in the TG process required

a high temperature around 150  $^{\circ}\text{C}$  due to the continuous increasing temperature and thermal hysteresis. SSR mainly decomposed in stage II (150–500  $^{\circ}\text{C}$ ) with approximately 71 wt% weight loss. Whereas in stage III (>500  $^{\circ}\text{C}$ ), the residue decomposed slowly and formed a porous char including ash. The final mass contents were 24.36–26.58 wt%, which agreed well with the total content of fixed carbon and ash of 23.54 wt% in the proximate analysis of SSR.

According to Fig. 1, there were two peaks in the DTG curves under lower heating rates, but only a main peak and a shoulder peak at 40  $^{\circ}\text{C min}^{-1}$ . This might be attributed to the fact that more volatiles were generated in a short time under higher heating rates. The first peak centered at 236.6  $^{\circ}\text{C}$  might be related to the decomposable compounds, like hemicellulose, fat, and so on. The main peak situated at 339.9  $^{\circ}\text{C}$  might result from the overlapping decomposition of lignin, cellulose or protein.<sup>31</sup> In addition, the relevant pyrolytic parameters of the main decomposition stage of SSR (stage II) are demonstrated in Table 2. The high heating rates were responsible for the enhanced mass loss rates. The maximum mass loss rate ( $\text{DTG}_{\text{max}}$ ) rose gradually from 3.27%  $\text{min}^{-1}$  to 21.37%  $\text{min}^{-1}$  as the heating rate rose from 5 to 40  $^{\circ}\text{C min}^{-1}$ .

### 3.3 Kinetic analysis

As typical equivalent conversion rate methods, the FWO and KAS methods are simple and possess good experimental linearity, regardless of the  $f(\alpha)$ . The pyrolysis kinetics of SSR were studied with the  $\alpha$  range of 0.1–0.7. Fig. 2 shows the corresponding plots of iso-conversional lines with high linear correlation coefficients (>0.98). The linear equations at different conversions show the corresponding activation energy ( $E$ ) values (Fig. 2c). Apparently, the  $E$  values calculated from both

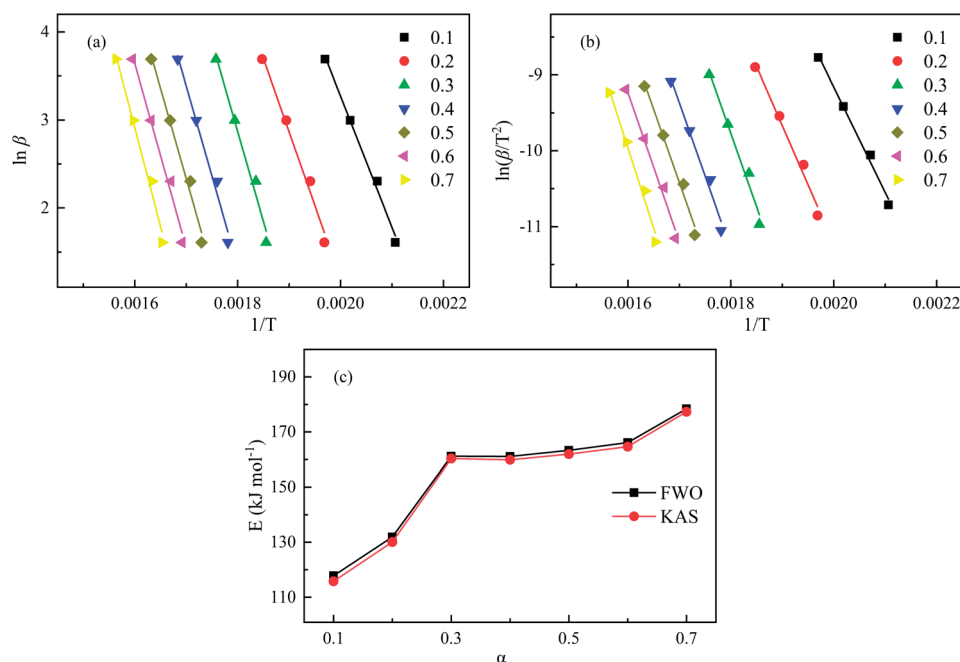


Fig. 2 Kinetic plots according to FWO (a) and KAS (b) and the corresponding activation energies (c) of SSR.

the FWO and KAS methods exhibited a monotonous increasing trend with  $\alpha$ , indicating that the SSR pyrolysis was a multi-step reaction and decomposing at higher  $\alpha$  was more difficult. The  $E$  values were about 117.81–178.4 kJ mol<sup>-1</sup> from FWO, and 115.77–177.33 kJ mol<sup>-1</sup> from KAS, within a variation of only 2.5 kJ mol<sup>-1</sup>, indicating that both methods were effective in determining the activation energy for SSR pyrolysis.

### 3.4 *Ex situ* CFP experiments via Py-GC/MS

**3.4.1 Effects of HZSM-5 on SSR pyrolysis performance.** The non-catalytic and *ex situ* CFP of SSR were executed to determine the catalytic influences of HZSM-5 on the product formation, the typical ion chromatograms are depicted in the ESI (Fig. S2†). In the non-catalytic SSR pyrolysis, various compounds were generated, including aromatic hydrocarbons, acids, linear carbonyls, anhydrosugars, phenolics and N-containing compounds, which derived from different components of SSR. Anhydrosugars and linear carbonyls were typical products from the depolymerization and ring scission of cellulose and hemicellulose of SSR.<sup>32,33</sup> The aromatic hydrocarbons and phenolics were not only derived from lignin, but also generated from the protein decomposition. In general, proteins consist of various amino acids with different side-chains, which were crucial to the formation of special products. As mentioned in our previous research,<sup>32</sup> the toluene could be derived from phenylalanine, while the phenol and indole were more likely the derivatives of tyrosine and tryptophan, respectively. Meanwhile, the abundant amine functional groups in the protein might be responsible for the generation of pyrrole by the Maillard reaction between the amino and carbonyl groups from protein and carbohydrates, respectively.<sup>32</sup> The fat in SSR was responsible for the generation of long-chain fatty acids, like oleic acid and linoleic acid. It is noted that dozens of products without any dominant ones could be derived from SSR pyrolysis, indicating the unsatisfactory selectivity in the non-catalytic process.

Differently from the pyrolysis of pure SSR, five major aromatic hydrocarbons became the predominant products from the *ex situ* CFP of SSR, which were benzene, toluene, xylene, naphthalene and methyl naphthalene. The first three products are monocyclic aromatic hydrocarbons (MAHs), while the latter two are polycyclic aromatic hydrocarbons (PAHs). This catalytic effect was attributed to the excellent shape selectivity and aromatization of HZSM-5, and coincided well with the previous literatures.<sup>28,34</sup> Therefore, it is interesting to explore the optimal pyrolytic conditions for maximizing the yields of aromatic hydrocarbons.

**3.4.2 Effects of HZ-to-SSR ratios on the generation of aromatic hydrocarbons.** The CFP of SSR was carried out at 650 °C under different HZ-to-SSR ratios of 5, 7, 9, 11 and 13, respectively, to determine the impact of HZSM-5 amount on the regulation of aromatic hydrocarbons. The aromatic hydrocarbons were quantified with the yields shown in Fig. 3. The non-catalytic process obtained very minor amounts of aromatic hydrocarbons, with a MAHs yield of 0.58 wt% and PAHs yield less than 0.10 wt%, and thus, the results are not shown here. Almost all the aromatic hydrocarbons had the maximum yields

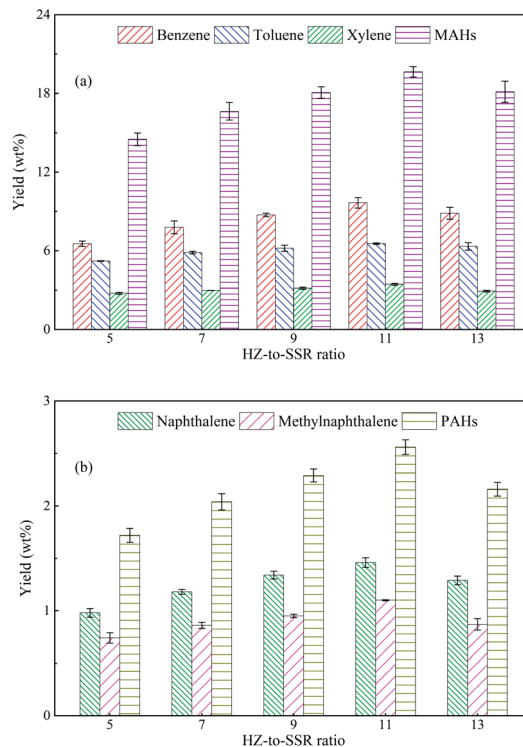


Fig. 3 Influences of HZ-to-SSR ratio on the aromatics yields from Py-GC/MS.

at the HZ-to-SSR ratio of 11, wherein the total yield of aromatic hydrocarbons was 22.20 wt%, of which the MAHs and PAHs yields were 19.64 wt% and 2.56 wt%, respectively. Specifically, the yields of benzene, toluene, and xylene were 9.66 wt%, 6.54 wt% and 3.44 wt%, while the yields of naphthalene and methyl naphthalene were 1.46 wt% and 1.10 wt%, respectively. Within a small HZSM-5 dosage, the pyrolytic volatiles could not fully contact the active sites. However, the overuse of catalyst would result in the longer exposition of pyrolysis vapors trapped in the catalyst pores, thereby promoting the cracking, cross-linking, charring and other reactions on the excessive active sites to generate permanent gases, coke and char.<sup>35</sup>

It is notable that the highest yields of aromatic hydrocarbons from the CFP of typical lignocellulosic biomass with HZSM-5 were reported to be no more than 11 wt% in previous studies<sup>15,36</sup> and our work.<sup>27</sup> The above results clearly indicated that SSR was more promising than the lignocellulosic biomass to be used for the preparation of aromatic hydrocarbons, with the yield around two times of that from lignocellulosic biomass. This should be attributed to the different chemical compositions between SSR and lignocellulosic biomass. SSR was the byproduct from the soy sauce fermentation process, and fermentation pretreatment could degrade the organic components to facilitate the decomposition of SSR,<sup>37</sup> resulting in more volatiles to be further converted into aromatics. Therefore, SSR could be a potential feedstock to produce aromatic hydrocarbons for industrial applications.

**3.4.3 Effects of pyrolysis temperature on the generation of aromatic hydrocarbons.** The *ex situ* CFP tests of SSR were

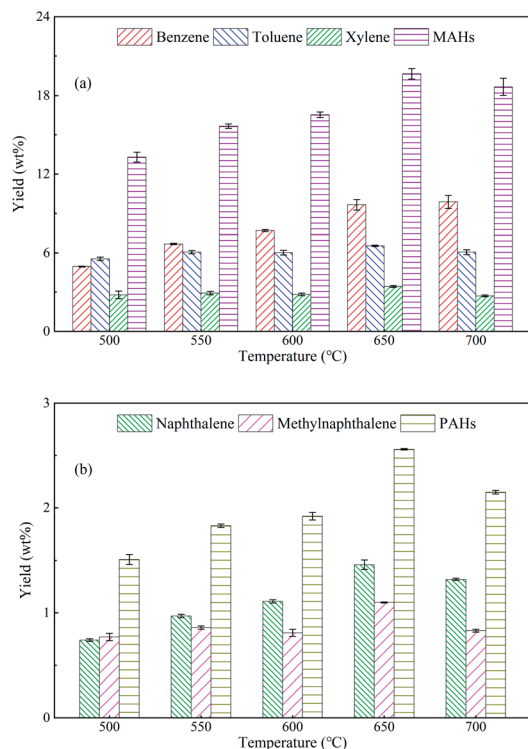


Fig. 4 Influences of pyrolysis temperature on the aromatic yields from Py-GC/MS.

further executed at an HZ-to-SSR ratio of 11 under various pyrolysis temperatures to determine the aromatic hydrocarbons distribution (Fig. 4). With the pyrolysis temperature rising from 500 °C to 650 °C, the MAHs and PAHs yields rose from 13.30 wt% and 1.51 wt% to 19.64 wt% and 2.55 wt%,

respectively. When the temperature increased to 700 °C, the MAHs and PAHs yields dropped to 18.66 wt% and 2.15 wt%, respectively. This confirmed that the production of aromatics required a high temperature (650 °C), in agreement with previous findings.<sup>38,39</sup> High temperatures could facilitate the decomposition of SSR as well as cracking, aromatization and other reactions over the HZSM-5, but extreme temperatures would induce the severe secondary reactions of pyrolytic vapors to generate gas or coke,<sup>27</sup> resulting in less volatiles to be further converted into aromatics.

### 3.5 *Ex situ* CFP experiments via the lab-scale device

Based on the Py-GC/MS experiments, the lab-scale CFP experiments of SSR with HZSM-5 were performed under 650 °C. The influences of the HZ-to-SSR ratio on the regulation of pyrolytic products were investigated (Fig. 5), wherein the HZ-to-SSR ratios were 0.5, 1, 1.5, 2, and 2.5, respectively. Compared with the pure SSR pyrolysis, HZSM-5 decreased the liquid yield and increased the gas yield obviously, accompanied with a slight increase of the solid yield. Such trends were further enhanced by the augmentation of HZ-to-SSR ratio. The liquid yield dropped from 49.92 wt% to 41.33 wt% as the HZ-to-SSR ratio increased from 0.5 to 2.5, while the gas yield rose from 23.59 wt% to 34.29 wt% monotonically. Moreover, the water content of the liquid product also rose along with the HZ-to-SSR ratio. Unlike the liquid and gas yields, the solid yield rose slightly from 22.96 wt% to 24.38 wt%. Since the CFP was carried out in the *ex situ* mode and the reaction temperature was fixed at 650 °C, the slight increase of the solid yield should mainly result from the coke deposition on HZSM-5.<sup>40</sup> During the *ex situ* CFP process, the devolatilization of SSR was mainly dependent on the pyrolysis temperature and the pyrolytic volatiles would contact the HZSM-5 and undergo various reactions over it to generate

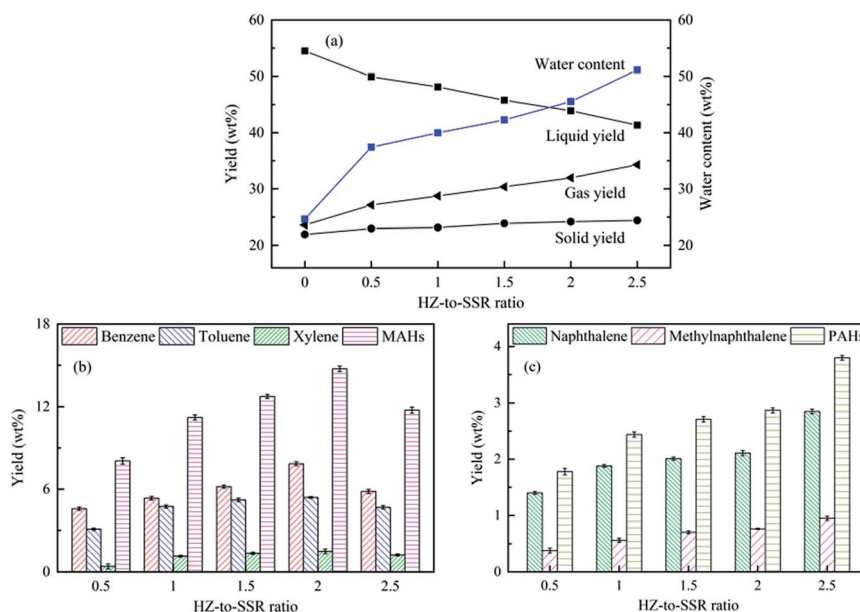


Fig. 5 Product distribution from lab-scale device at 650 °C with different HZ-to-SSR ratios.

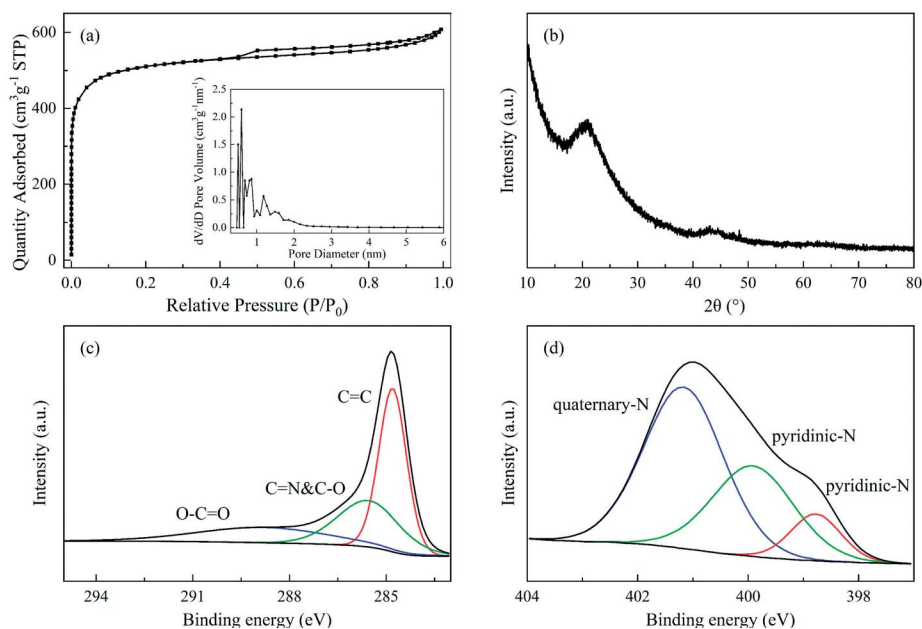


Fig. 6 (a)  $N_2$ -sorption isotherm, (b) XRD pattern, (c) C 1s spectrum, and (d) N 1s spectrum of NAC.

light organic volatiles (mainly aromatic hydrocarbons), water, permanent gases and char/coke. Under a fixed pyrolysis temperature, the catalyst and reaction time were critical for the catalysis process to generate the final products. Larger amounts of catalysts would provide more active sites and increase the vapor residence time, and as a result, more water, permanent gases and solid products were generated at the expense of organic liquid products.<sup>40,41</sup>

The yields of aromatic hydrocarbons are depicted in Fig. 5. Under the non-catalytic condition, the aromatics yield from pure SSR was too low to be accurately quantified, and the relevant results are not given. As demonstrated in Fig. 5b, the MAHs yield had a tendency of increasing first and then decreasing with the increase of the HZ-to-SSR ratio, similar to the results from the Py-GC/MS above. The yields of aromatic hydrocarbons and MAHs had maximum values of 17.61 wt% and 14.74 wt%, respectively, including 7.85 wt% benzene, 5.40 wt% toluene and 1.49 wt% xylene. In addition, the PAHs yield rose monotonically from 1.78 wt% to 3.80 wt% as the HZ-to-SSR ratio rose from 0.5 to 2.5, which might be resulted from the enhanced reactions of MAHs with other oxygenated compounds to generate PAHs under high HZ-to-SSR ratios.<sup>42</sup> PAHs are known as undesirable compounds due to their high toxicity, and they are also the precursors of coke.

Therefore, high HZ-to-SSR ratios should not be used in the CFP of SSR to avoid the significant formation of PAHs.

### 3.6 Physicochemical properties of NAC

In order to improve the economy of the CFP technology of SSR, the pyrolytic solid product obtained at the optimum condition was activated for the co-production of NAC. The porous properties as well as XRD and XPS analysis results of NAC are illustrated in Fig. 6 and Table 3. Based on the IUPAC nomenclature, the  $N_2$  sorption isotherm plots of NAC in Fig. 6a belonged to type-IV, which exhibited the fingerprints of both microporosity and mesoporosity.<sup>43</sup> The inset figure in Fig. 6a further demonstrated that the NAC was dominated by micropores with an average pore diameter of 1.90 nm. As shown in Table 3, the corresponding SSA and total pore volume were  $1928.6 \text{ m}^2 \text{ g}^{-1}$  and  $0.932 \text{ cm}^3 \text{ g}^{-1}$ , of which the micropores contributed 70.4% and 57.4%, respectively. The high salt content that remained in the solid product should contribute to the formation of the hierarchical pores of NAC during the activation process,<sup>28</sup> which would be instrumental in the ion transfer and charge storage.<sup>10,44</sup>

As demonstrated in Fig. 6b, a prominent diffraction peak centered at  $21.2^\circ$  and a weak peak at  $43.2^\circ$  emerged in the XRD

Table 3 Pore properties and elemental composition of NAC

SSA ( $\text{m}^2 \text{ g}^{-1}$ )		Pore volume ( $\text{cm}^3 \text{ g}^{-1}$ )		Diameter (nm)	Elemental composition (wt%)			
$S_{\text{BET}}$	$S_{\text{mic}}^a$	$V_{\text{total}}^b$	$V_{\text{mic}}^c$	$D_{\text{average}}$	C	H	O	N
1928.6	1358.6	0.932	0.535	1.90	82.64	0.58	14.67	1.60

<sup>a</sup> t-Plot micropore area. <sup>b</sup>  $P/P_0 = 0.989$ . <sup>c</sup> t-Plot micropore volume.

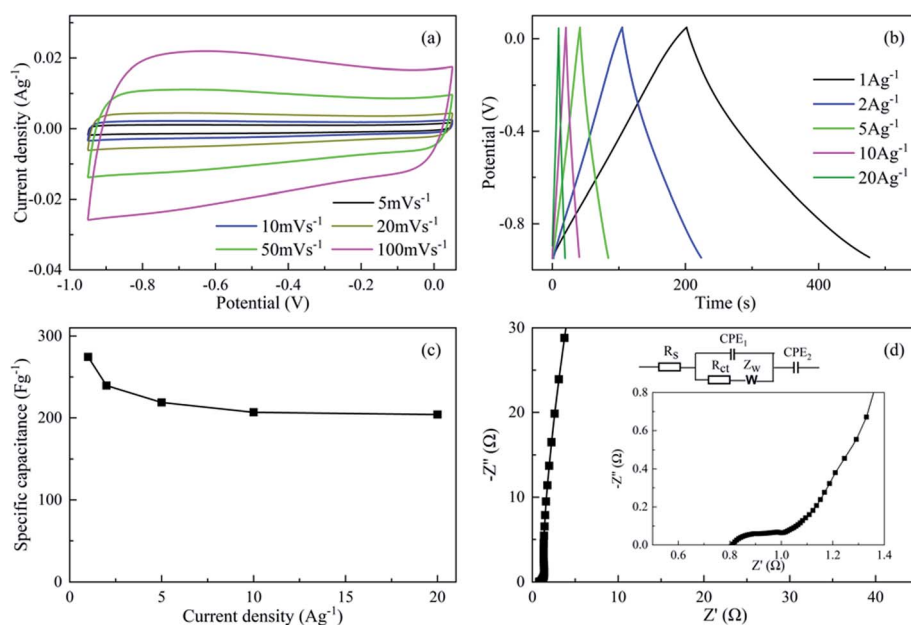


Fig. 7 (a) CV curves, (b) GCD plots, (c)  $C_g$ s and (d) Nyquist plots of NAC.

spectrum of NAC. The former was ascribed to the (002) plane, while the latter was to the (100) plane. The (002) plane peak usually appears at approximately  $22.5^\circ$  so the shift of the peak in NAC towards a lower angle was believed to be due to the high N and O contents in NAC.<sup>23</sup> This can be verified by the ultimate analysis demonstrated in Table 3, in which the N and O contents were 1.60 wt% and 14.67 wt%, respectively. Moreover, the predominant broad diffraction peak revealed the graphitization of NAC to some extent.<sup>45</sup>

The XPS spectra of C 1s and N 1s of NAC are demonstrated in Fig. 6c and d. The peaks situated at 284.8, 285.5 and 288.8 eV could be attributed to C=C, C=N/C-O, and O-C=O, respectively. For the N species, three peaks situated at 398.7, 399.9, and 401.1 eV represented pyridinic-N, pyrrolic-N and quaternary-N, respectively. The capacitance of NAC consisted of pseudocapacitance and weight capacitance. The presence of pyridinic-N, pyrrolic-N and C=O would enhance the pseudocapacitance of NAC, while the existence of quaternary-N would augment the weight capacitance of NAC.<sup>24,46</sup>

### 3.7 Electrochemical characteristics

The CV, GCD and EIS results of NAC are illustrated in Fig. 7. All the CV curves of NAC possessed quasi-rectangular shapes (Fig. 7a), implying the high electron ion transfer rate and low inner resistance of NAC.<sup>47</sup> The GCD curves of NAC under various current densities exhibited non-linear characteristics, which might be attributed to the extra pseudocapacitance donated by heteroatom-doped groups. Furthermore, the corresponding  $C_g$ s were calculated (Fig. 7c). Apparently, the  $C_g$  exhibited a tendency of monotonically decreasing with the increase of current densities. The  $C_g$  achieved a satisfactory value of  $274.5 \text{ F g}^{-1}$  at  $1 \text{ A g}^{-1}$  and decreased to  $204.0 \text{ F g}^{-1}$  at  $20 \text{ A g}^{-1}$  with a 74.3%  $C_g$  retention. The reduction of the  $C_g$

under high current densities might be ascribed to the large impedance caused by the micropores.<sup>48</sup> Generally, large impedance would increase the charging time constant to complete charge, leading to the incomplete charge and decrease of  $C_g$ . The high retention implied the excellent electrochemical capacitive properties, which might be ascribed to the synergistic effects of the good pore structure and effective incorporation of N in the NAC.<sup>22</sup>

According to the Nyquist plot of NAC in Fig. 7d, the large line slope in the low frequency region implied the good capacitive behavior of NAC with a low diffusion resistance in the pores.<sup>24</sup> The semicircle at high frequencies demonstrated that the NAC possessed a low charge transfer resistance ( $R_{ct}$ ) of no more than  $0.2 \Omega$  and equivalent series resistance ( $R_s$ ) of approximately  $0.8 \Omega$ , suggesting the excellent conductivity of NAC.<sup>49</sup> In addition, a low Warburg impedance ( $Z_w$ ) of  $0.9 \Omega$  was attained, indicating that electrolyte ions were permitted access to the electrode surface efficiently through a short ion diffusion path. In brief, the synergistic effects of the heteroatom incorporation and hierarchical pores enabled the NAC to be promising as a supercapacitor because the heteroatom-containing groups would facilitate the extra pseudocapacitance as well as the wettability, while the hierarchical pores could enhance the ion transfer and charge storage.

## 4. Conclusions

The present work provided a creative method for the poly-generation of aromatic hydrocarbons and NAC from the *ex situ* CFP of SSR with HZSM-5. The pyrolysis of SSR without the catalyst generated various complex pyrolytic products without any dominant ones due to the complicated composition of SSR, which mainly includes protein, fat, cellulose, hemicellulose,



lignin and salt. The presence of HZSM-5 for the *ex situ* CFP of SSR could achieve the selective preparation of aromatic hydrocarbons and moreover, the pyrolytic solid product could be further activated with KOH without an extra N source to produce NAC as a supercapacitor electrode material. The results indicated that the CFP of SSR with HZSM-5 at 650 °C favored the selective preparation of aromatic hydrocarbons. The maximum yield of aromatic hydrocarbons reached 22.20 wt% from Py-CG/MS with an HZ-to-SSR ratio of 11, consisting of 19.64 wt% MAHs and 2.56 wt% PAHs, respectively. In addition, the lab-scale test obtained 17.61 wt% aromatic hydrocarbons with 14.74 wt% MAHs and 2.87 wt% PAHs at an HZ-to-SSR ratio of 2. The aromatic hydrocarbon yields were much higher than those produced from typical lignocellulosic materials with HZSM-5 (<11 wt%). In addition, the prepared NAC possessed hierarchical pores incorporated with N and exhibited an excellent  $C_g$  of 274.5 F g<sup>-1</sup> at 1 A g<sup>-1</sup>.

## Conflicts of interest

There are no conflicts to declare.

## Acknowledgements

The authors thank the National Natural Science Foundation of China (51906066, 51922040), Grants from Fok Ying Tung Education Foundation (161051) and Fundamental Research Funds for the Central Universities (2020DF01, 2019JG002, 2018ZD08) for financial support.

## References

- 1 C. Xiang, S. Y. Liu, Y. Fu and J. Chang, *Renewable Energy*, 2019, **134**, 739–744.
- 2 P. Chen, H. Song, Y. Wang, P. Chen, X. Shen and S. Yao, *J. Mater. Cycles Waste Manage.*, 2015, **17**, 574–582.
- 3 X. Chen, Y. Luo, B. Qi, J. Luo and Y. Wan, *Ultrason. Sonochem.*, 2017, **35**, 351–358.
- 4 X. Chen, Y. Luo, B. Qi and Y. Wan, *Sep. Purif. Technol.*, 2014, **128**, 72–79.
- 5 Q. Lu, Z. Zhang, C. Dong and X. Zhu, *Energies*, 2010, **3**, 1805–1820.
- 6 C. Liu, H. Wang, A. M. Karim, J. Sun and Y. Wang, *Chem. Soc. Rev.*, 2014, **43**, 7594–7623.
- 7 Z. Zhang, K. Li, S. Ma, M. Cui, Q. Lu and Y. Yang, *Ind. Crops Prod.*, 2019, **137**, 495–500.
- 8 C. Liang, G. Gascó, S. Fu, A. Méndez and J. Paz-Ferreiro, *Soil Tillage Res.*, 2016, **164**, 3–10.
- 9 M. Li and R. Xiao, *Fuel Process. Technol.*, 2019, **186**, 35–39.
- 10 J. K. Kim, Y. Yoo and Y. C. Kang, *Chem. Eng. J.*, 2020, **382**, 122805.
- 11 Q. Lu, Z. Wang, H. Guo, K. Li, Z. Zhang, M. Cui and Y. Yang, *Fuel*, 2019, **243**, 88–96.
- 12 Q. Lu, M. Zhou, W. Li, X. Wang, M. Cui and Y. Yang, *Catal. Today*, 2018, **302**, 169–179.
- 13 L. Zhu, Y. Zhang, H. Lei, X. Zhang, L. Wang, Q. Bu and Y. Wei, *Sustainable Energy Fuels*, 2018, **2**, 1781–1790.
- 14 W. Chen, X. Wang, M. Luo, P. Yang and X. Zhou, *Waste Manag.*, 2019, **89**, 129–140.
- 15 Nishu, R. Liu, M. M. Rahman, M. Sarker, M. Chai, C. Li and J. Cai, *Fuel Process. Technol.*, 2020, **199**, 106301.
- 16 D. J. Mihalcik, C. A. Mullen and A. A. Boateng, *J. Anal. Appl. Pyrol.*, 2011, **92**, 224–232.
- 17 S. Thangalazhy-Gopakumar, S. Adhikari, S. A. Chattanathan and R. B. Gupta, *Bioresour. Technol.*, 2012, **118**, 150–157.
- 18 Z. Li, L. Zhang, B. S. Amirkhiz, X. Tan, Z. Xu, H. Wang, B. C. Olsen, C. M. Holt and D. Mitlin, *Adv. Eng. Mater.*, 2012, **2**, 431–437.
- 19 H. Lu and X. S. Zhao, *Sustainable Energy Fuels*, 2017, **1**, 1265–1281.
- 20 X. Zhao, C. Yan, X. Gu, L. Li, P. Dai, D. Li and H. Zhang, *Chemelectrochem*, 2017, **4**, 1516–1522.
- 21 J. Wang, Y. Li, L. Yan and Y. Qu, *Int. J. Electrochem. Sci.*, 2018, **13**, 6259–6271.
- 22 D. Xu, Y. Su, S. Zhang and Y. Xiong, *Energy Sources, Part A*, 2020, **42**, 1797–1807.
- 23 C. J. Raj, M. Rajesh, R. Manikandan, K. H. Yu, J. Anusha, J. H. Ahn, D.-W. Kim, S. Y. Park and B. C. Kim, *J. Power Sources*, 2018, **386**, 66–76.
- 24 C. Lu, Y. H. Huang, Y. J. Wu, J. Li and J. P. Cheng, *J. Power Sources*, 2018, **394**, 9–16.
- 25 P. A. Alaba, S. I. Popoola, F. Abnisa, C. S. Lee, O. S. Ohunakin, E. Adetiba, M. B. Akanle, M. F. A. Patah, A. A. A. Atayero and W. M. A. W. Daud, *J. Therm. Anal. Calorim.*, 2020, **140**, 1181–1823.
- 26 P. A. Alaba, Y. M. Sani and W. M. A. W. Daud, *J. Therm. Anal. Calorim.*, 2016, **126**, 943–948.
- 27 K. Li, Z.-x. Wang, G. Zhang, M.-s. Cui, Q. Lu and Y.-p. Yang, *Sustainable Energy Fuels*, 2020, **4**, 538–548.
- 28 C. Wang, D. Wu, H. Wang, Z. Gao, F. Xu and K. Jiang, *J. Mater. Chem. A*, 2018, **6**, 1244–1254.
- 29 J. Alvarez, M. Amutio, G. Lopez, L. Santamaria, J. Bilbao and M. Olazar, *Waste Manag.*, 2019, **85**, 385–395.
- 30 C. S. Fermanelli, A. Córdoba, L. B. Pierella and C. Saux, *Waste Manag.*, 2020, **102**, 362–370.
- 31 F. Tang, Z. Yu, Y. Li, L. Chen and X. Ma, *Bioresour. Technol.*, 2020, **299**, 122636.
- 32 K. Li, L. Zhang, L. Zhu and X. Zhu, *Bioresour. Technol.*, 2017, **234**, 48–52.
- 33 S. Wang, G. Dai, H. Yang and Z. Luo, *Prog. Energy Combust. Sci.*, 2017, **62**, 33–86.
- 34 A. López, I. De Marco, B. Caballero, A. Adrados and M. Laresgoiti, *Waste Manag.*, 2011, **31**, 1852–1858.
- 35 M. Zhang and A. Moutsoglou, *Energy Fuels*, 2014, **28**, 1066–1073.
- 36 Q. Che, M. Yang, X. Wang, Q. Yang, L. R. Williams, H. Yang, J. Zou, K. Zeng, Y. Zhu and Y. Chen, *Bioresour. Technol.*, 2019, **278**, 248–254.
- 37 T. Kan, S. Grierson, R. Nys and V. Strezov, *Energy Fuels*, 2014, **28**, 104–114.
- 38 P. Qi, G. Chang, H. Wang, X. Zhang and Q. Guo, *J. Anal. Appl. Pyrol.*, 2018, **136**, 178–185.
- 39 X. Ren, J. Cao, X. Zhao, W. Shen and X. Wei, *J. Anal. Appl. Pyrol.*, 2018, **130**, 190–197.

- 40 B. Muneer, M. Zeeshan, S. Qaisar, M. Razzaq and H. Iftikhar, *J. Cleaner Prod.*, 2019, **237**, 117762.
- 41 N. H. Zainan, S. C. Srivatsa, F. Li and S. Bhattacharya, *Fuel*, 2018, **223**, 12–19.
- 42 S. Liu, Y. Zhang, L. Fan, N. Zhou, G. Tian, X. Zhu, Y. Cheng, Y. Wang, Y. Liu, P. Chen and R. Ruan, *Fuel*, 2017, **196**, 261–268.
- 43 M. Thommes, K. Kaneko, A. V. Neimark, J. P. Olivier, F. Rodriguez-Reinoso, J. Rouquerol and K. S. Sing, *Pure Appl. Chem.*, 2015, **87**, 1051–1069.
- 44 W. Chen, X. Wang, C. Liu, M. Luo, P. Yang and X. Zhou, *Waste Manag.*, 2020, **102**, 330–339.
- 45 Z. Zou and C. Jiang, *J. Alloys Compd.*, 2020, **815**, 152280.
- 46 D. Fu, Z. Chen, C. Yu, X. Song and W. Zhong, *Prog. Nat. Sci.*, 2019, **29**, 495–503.
- 47 K. Li, W. Chen, H. Yang, Y. Chen, S. Xia, M. Xia, X. Tu and H. Chen, *Bioresour. Technol.*, 2019, **280**, 260–268.
- 48 P. Divya and R. Rajalakshmi, *J. Energy Storage*, 2020, **27**, 101149.
- 49 J. Yang, Y. Wang, J. Luo and L. Chen, *Ind. Crops Prod.*, 2018, **121**, 226–235.